Synergistic integration of energy storage catalysis: A multifunctional catalytic material for round-the-clock environmental cleaning

Min Wang [a,b], Guoqiang Tan [a,*], Bixin Zhang [a], Yong Wang [a], Yu Bi [a], Qian Yang [a], Ying Liu [a], Tian Liu [a], Zeqiong Wang [a], Huijun Ren [c], Long Lv [d], Ao Xia [a], Lixiong Yin [a], Qibin Yuan [e], Wenlong Liu [e], Yun Liu [e]

[a] *Shaanxi Key Laboratory of Green Preparation and Functionalization for Inorganic Materials, School of Materials Science and Engineering, Shaanxi University of Science & Technology, Xi'an 710021, China*
[b] *Department of Applied Chemistry, Yuncheng University, Yuncheng 044000, China*
[c] *School of Arts and Sciences, Shaanxi University of Science & Technology, Xi'an 710021, China*
[d] *College of Cryptography Engineering, Engineering University of PAP, Xi'an 710086, China*
[e] *School of Electronic Information and Artificial Intelligence, Shaanxi University of Science & Technology, Xi'an 710021, China*

ARTICLE INFO

ABSTRACT

A round-the-clock $Ag/BiO_{2-x}/Bi_2O_{2.75}$ energy storage catalyst with the unique electron-hole storage mechanism is prepared by natural photo-deposition method. Ag is directional deposited on the surface of BiO_{2-x} due to the Z-scheme mechanism, and electrons and holes are severally stored in Ag and $Bi_2O_{2.75}$. The recombination of electron-hole pairs is efficiently suppressed owing to the formation of Schottky junction, and the capacitance nature of Ag, leading to that the concentrations of the stored electrons and holes are markedly increased from 24.94 and 0.0042 $\mu mol \cdot g^{-1}$ to 86.55 and 0.0481 $\mu mol \cdot g^{-1}$. Hence, $Ag/BiO_{2-x}/Bi_2O_{2.75}$ shows the boosted and long-lasting dark catalytic activity for organic pollutants mineralization, meanwhile possessing appealing structural stability, recyclability and repairability. Furthermore, the generation of the reactive oxygen species is promoted and NO oxidation pathway is changed due to the light-induced surface plasmon resonance effect of the stored electrons and holes and the resultant near-field enhancement effect, resulting in the significantly enhanced full-spectrum photocatalytic performance for antibiotic degradation and NO deep oxidation. This work may open up new horizons for the design and preparation of high-active round-the-clock catalytic materials.

1. Introduction

Photocatalytic technology is regarded as a feasible strategy to manage environmental crisis by utilizing green and renewable solar energy [1]. In comparison with the traditional techniques, the photocatalytic technology exhibits the unique advantages of low energy consumption, mild reaction conditions, and so on. Despite, the practical application of photocatalytic technology still remains the great challenges owing to the intermittent and regional characteristics of solar energy. For some special areas and occasions that require all-day environmental cleaning, such as hospitals, photocatalytic technology is hindered because the catalytic reactions cannot be continuously performed in dark [2,3]. Hence, the round-the-clock catalysts need to be designed and prepared to solve practical issues [4,5].

In addition to meeting the fundamental requirements of photo-reactions, energy storage medium is essential for the round-the-clock catalysts. Dark catalytic reactions generally depend on the photo-induced charge and dark-discharge processes of the energy storage medium. Therefore, the round-the-clock catalysts can be regarded as the organic combination of energy storage and catalysis. Redox pairs are the most common energy storage medium. Due to the reversible cycle of redox pairs during light-dark reactions, such as Pd^{2+}/Pd^0, Cu^{2+}/Cu^+, Co^{3+}/Co^{2+}, W^{6+}/W^{5+}, Bi^{5+}/Bi^{3+}, Mo^{6+}/Mo^{5+}, Sn^{4+}/Sn^{2+}, Li et al. prepared N-TiO_2/PdO [6], $SrCu_xO$ composite [7], CeSrCoO perovskite [8], TiO_2/WO_3 QDs [9], $NaBiO_3/BiO_{2-x}$ [10], Mo-doped TiO_2 [11], SnO_2/Cu_2O [12] all exhibited the obvious dark catalytic performance for organic pollutant degradation, bacterial inactivation and hydrogen production.

Moreover, noble metals (Au, Ag and Pt) can also act as the energy storage medium for the preparation of the round-the-clock catalysts [2,

---

* Corresponding author.
E-mail address: tan3114@163.com (G. Tan).

3,13–17]. Takai et al. [18] systematically investigated the electron storage capacity of redox pairs (Ti^{4+}/Ti^{3+}), Au, Ag and Pt. After UV irradiation, the electron storage concentrations in TiO_2, Ag/TiO_2, Au/TiO_2 and Pt/TiO_2 were 63, 440, 280 and 190 $\mu mol \cdot L^{-1}$, respectively. The relatively higher electron storage concentration in Ag/TiO_2 is attributed to the capacitance nature of Ag [19], which means that the long-term electron storage can be achieved by introducing Ag into the material system. Unfortunately, the dark catalytic activity of redox pairs- and metal-mediated catalysts need to be activated by the complex pre-illumination treatment or adding extra co-catalysts. Due to the existence of abundant localized electrons, oxygen vacancies-modified catalysts usually exhibit the remarkably enhanced activation ability for the adsorbed oxygen species, resulting in that the dark reaction can be directly driven without pre-illumination treatment with the assistance of an appropriate co-catalyst [20–22].

Generally, dark catalytic reaction can only maintain one reaction period owing to the low energy storage efficiency of redox pairs, metals and oxygen vacancies. Long-lasting dark catalytic activity can be achieved by coupling Ag with oxygen vacancies-modified $NaBiO_3$ [23]. Nevertheless, the extremely poor structural stability of $NaBiO_3$ limits its potential application. Moreover, up to now, the reported round-the-clock catalytic materials all exhibit the single electron storage mechanism, as listed in Table S1, and the active hole is almost incapable of participating in dark reactions.

Recently, Z-scheme heterojunction has aroused wide concern in the field of photocatalysis. Unlike conventional I-type or II-type heterojunctions, for Z-scheme heterojunction, the photogenerated electrons and holes with the strong redox capabilities are retained, and the redox reactions can independently occur on different semiconductor surface [24,25]. Nevertheless, the photo-generated carriers still cannot be long-termly stored in the heterojunctions in dark owing to the fast recombination of electron-hole pairs induced by Coulomb interactions. If the photo-generated electrons of the Z-scheme heterojunction can be extracted into Ag with capacitive properties, the photo-generated holes with strong oxidizing ability can be retained in the heterojunction for a long time. In short, the unique electron-hole storage mechanism and long-lasting dark catalytic performance can be simultaneously achieved by coupling Ag with Z-scheme heterojunction. Furthermore, Ag shows the obvious localized surface plasmon resonance (LSPR) effect [26]. Upon illumination, the free electrons of Ag oscillate coherently with incident photons, which can not only induce the generation of high-energy hot carriers, but also broaden the light absorption to full-spectrum range. And the resultant localized near-field enhancement can accelerate electron transition and promote interfacial charge transfer. Therefore, for Ag coupling Z-scheme heterojunction, the formation of electron-hole storage mechanism can efficiently facilitate light-induced LSPR effect and photochemical reactions [27–29], which is a win-win strategy to simultaneously improve the full-spectrum responsive photocatalytic and dark catalytic activities.

Hence, we report a round-the-clock catalyst with unique electron-hole storage mechanism, which is consist of Ag and Z-scheme $BiO_{2-x}/Bi_2O_{2.75}$ heterojunction, and is prepared via natural photo-deposition method. Ag is directional deposited on the surface of BiO_{2-x} due to the Z-scheme mechanism, and electrons and holes are severally stored in Ag and $Bi_2O_{2.75}$. The energy storage efficiency of $Ag/BiO_{2-x}/Bi_2O_{2.75}$ is markedly improved since the recombination of electron-hole pairs is inhibited owing to the formation of Schottky junction at Ag/BiO_{2-x}, and the capacitance nature of Ag, resulting in the enhanced and long-lasting dark catalytic activity. $Ag/BiO_{2-x}/Bi_2O_{2.75}$ also shows the boosted full-spectrum photocatalytic activity due to the accelerated electron transition and interfacial charge transfer induced by LSPR effect. Moreover, the possible enhancement mechanism of round-the-clock catalytic reaction is proposed.

2. Experimental section

2.1. Preparation of catalysts

2.1.1. Preparation of $BiO_{2-x}/Bi_2O_{2.75}$

$BiO_{2-x}/Bi_2O_{2.75}$ is prepared by hydrothermal reaction using $NaBiO_3$ (analytical reagent) as raw materials [30]. First, 1 mmol of $NaBiO_3$ was dispersed in 20 mL 3.0 $mol \cdot L^{-1}$ NaOH solution, and a homogeneous suspension was obtained after magnetic stirring for 20 min. The obtained suspension was further dispersed in 20 mL of deionized water, and the reaction precursor was obtained after magnetic stirring for 20 min. The obtained reaction precursor was transferred to a 50 mL Teflon-lined stainless-steel reactor and heated at 180 °C for 40 min. After cooling to room temperature, the obtained precipitate was washed with deionized water and ethanol for six times, and dried at 70 °C for 12 h. The attained $BiO_{2-x}/Bi_2O_{2.75}$ was named as BiO-OVs.

2.1.2. Preparation of $Ag/BiO_{2-x}/Bi_2O_{2.75}$

$Ag/BiO_{2-x}/Bi_2O_{2.75}$ was prepared via the natural photo-deposition method. The reaction system was exposed to a normal laboratory environment at room temperature, and a 36 W fluorescent tube (T8, FSL, 220 V) was used as the illumination light source and reaction light source, which was located 2 m directly above the experiment table. In addition to this, no other external light source was used. The detailed preparation process was as follows: Typically, 0.3 g of the prepared $BiO_{2-x}/Bi_2O_{2.75}$ powder was dispersed to 30 mL deionized water, and magnetically stirred for 30 min under natural light irradiation for 30 min. At the same time, a certain amount of $AgNO_3$ powder (analytical reagent) was dissolved in 30 mL of deionized water, and a transparent uniform solution was obtained after ultrasonic treatment for 30 min. Then, $AgNO_3$ solution was slowly added dropwise to the above $BiO_{2-x}/Bi_2O_{2.75}$ suspension, and magnetically stirred for 2 h under natural light irradiation. The obtained precipitate was washed with deionized water and ethanol for six times, and dried at 70 °C for 120 h. When the mass ratio of $AgNO_3$ to $BiO_{2-x}/Bi_2O_{2.75}$ were 1:20, 1:10, 3:20, 1:5, 1:4 and 3:10, the obtained $Ag/BiO_{2-x}/Bi_2O_{2.75}$ were named as AgBO-1, AgBO-2, AgBO-3, AgBO-4, AgBO-5 and AgBO-6, respectively.

2.2. Characterization

X-ray diffraction (XRD) patterns were recorded by D/max-2200PC diffraction with Cu kα radiation (λ = 0.15418 nm). Raman spectra were recorded by Renishaw Raman spectrometer with the excitation wavelength of 532 nm. Scanning electron microscope (SEM, FEI Verios 460) and (high-resolution) transmission electron microscope (TEM (HRTEM), FEI-Tecnai, G2 F20) were used to observe the micromorphology of the catalysts. N_2 adsorption-desorption isotherm curves were measured by 3 H-2000BET-A instrument. X-ray photoelectron spectra (XPS) were recorded by Model XSAM800 X-ray photoelectron spectrometer. Ultraviolet-visible-near infrared diffuse reflectance spectra (UV–vis NIR DRS) were obtained by Agilent Cary 5000 spectrophotometer. Electron paramagnetic resonance (EPR) spectra were recorded by Bruker a300 spectrometer. Fourier transform infrared (FT-IR) spectra were obtained by VECTOR-22 spectrometer. Temperature programmed desorption (TPD) curves were recorded by AutoChem1 II chemical adsorption instrument.

2.3. Dark catalytic experiments

Dark catalytic performance of the catalysts were evaluated by degrading organic pollutants in dark, including tetracycline (TC, 20 $mg \cdot L^{-1}$), ciprofloxacin (CIP, 5 $mg \cdot L^{-1}$), bisphenol A (BPA, 10 $mg \cdot L^{-1}$), acid red (AR, 20 $mg \cdot L^{-1}$), methyl orange (MO, 10 $mg \cdot L^{-1}$) and rhodamine B (RhB, 5 $mg \cdot L^{-1}$). Typically, 50 mg of the catalyst was dispersed into 50 mL of the pollutant solution, which was placed in an XPA-7 photochemical reactor. The surrounding of the reactor was closed

to ensure completely dark reaction conditions. Then, the magnetic stirring (1000 r•min^{-1}), and 2 mL of the suspension was taken at regular interval. The suspension was filtered with a 0.22 μm NYLON filter head to remove catalyst powder. The concentration of the residual organic pollutant in the supernatant was measured by UV–vis spectrophotometer (SP-756 P). The stability, reusability and repairability of the catalyst in the dark were characterized by cycle experiments, and the detailed operational process was available in Supporting Information. Active species trapping experiments were carried out with sodium bromate (NaBrO$_3$), sodium oxalate (Na$_2$C$_2$O$_4$), p-benzoquinone (BQ) and tertiary butanol (tBuOH) as the sacrificial agents of e$^-$, h$^+$, •O$_2^-$ and •OH radicals, respectively. The mineralization rate and decomposition products of the organic pollutant in dark were analyzed by total organic carbon (TOC) measurement and liquid chromatography-tandem mass spectrometry (LC-MS) technology.

2.4. Photocatalytic experiments

Photocatalytic TC degradation: The photocatalytic activity of the catalyst was first evaluated by degrading TC (20 mg•L^{-1}) under simulated sunlight (500 W Xenon lamp, 190 nm $<\lambda<$ 1100 nm) and NIR light (500 W Xenon lamp equipped with the corresponding filters, 800 nm $<\lambda$ $<$ 1500 nm). The experimental operation was similar to the dark catalytic reaction.

Photocatalytic NO removal: The photocatalytic performance of the catalyst was further evaluated by removing NO under simulated sunlight irradiation (300 W Xenon lamp). First, 50 mg of the catalyst was dispersed in 10 mL of absolute ethanol with a petri dish (R=3 cm) as the container, and ultrasonic treatment for 15 min. After drying, the obtained sample was placed in a cylindrical reactor (R=5 cm, H=10 cm) with a quartz glass cover. NO and compressed air were continuously injected into the reactor with the flow rate of 1.5 and 0.285 L·min^{-1}, respectively. After the adsorption-desorption equilibrium was reached, the concentration of NO in the mixed gas was stabilized at about 600 ppb, and the relative humidity was approximately 45%. Then, the xenon lamp was turned on. During the photocatalytic reaction, the relative humidity of the reaction system decreased slightly (in the range of 20%−30%) due to the consumption of H$_2$O. During the dark-adsorption and photo-reaction, the real-time NO and NO$_2$ concentration was recorded by a chemiluminescence NO analyzer (Thermo Scientific, 42i). Active species trapping experiments were performed using potassium dichromate (K$_2$Cr$_2$O$_7$), potassium iodide (KI), BQ, tBuOH, catalase (CAT) and β-carotene (β-CAR) as the scavengers of e$^-$, h$^+$, •O$_2^-$, •OH, H$_2$O$_2$ and ^{1}O$_2$, respectively. NO oxidation products and reaction pathways were analyzed by in-situ FT-IR spectra.

2.5. Photo-electrochemical measurements

The photo-electrochemical measurements were carried out on an electrochemical workstation (CHI660E) equipped with a standard three-electrode cell system. Pt sheet, KCl saturated Ag/AgCl and FTO conducting glass were used as the counter electrode, reference electrode and working electrode, respectively. The working electrode was prepared as follows: 0.02 g of the catalyst was dispersed into the mixed solution of 1 mL of ethyl alcohol and 0.2 mL of film-forming reagent. After ultrasonic treatment for 30 min, a uniform suspension was obtained, which was coated on a FTO conducting glass (2 ×1.5 cm^2) and dried under ambient condition. Linear sweep voltammetry (LSV) curves, electrochemical impedance spectrum (EIS) and transient photocurrent response were measured under simulated sunlight irradiation. A 300 W Xenon lamp was used as simulated sunlight source, and 0.1 mol•L-1 of Na$_2$SO$_4$ solution was used as the electrolyte.

3. Results and discussion

3.1. Structural characterization and formation mechanism

Ag/BiO$_{2-x}$/Bi$_2$O$_{2.75}$ catalyst with the unique electron-hole storage mechanism is successfully prepared by natural light deposition method, and the corresponding formation mechanism is illustrated in Fig. 1. First, BiO$_{2-x}$/Bi$_2$O$_{2.75}$ heterojunction (BiO-OVs) is synthesized by hydrothermal reaction, and Bi$_2$O$_{2.75}$ nanoparticles are closely attached to the surface of BiO$_{2-x}$ nanosheets [30], as shown in the SEM image (Fig. S1(a)). According to the previous reports [30,31], the prepared BiO-OVs heterojunction shows the satisfactory dark-full-solar-spectrum reactive activation and Z-scheme mechanism due to the existence of oxygen vacancies and the resulting formation of the build-in polarization electric field (BIPEF) in Bi$_2$O$_{2.75}$, as depicted in Fig. 1(a).

Under natural light irradiation, BiO-OVs is excited due to its full-solar-spectrum absorption properties. Owing to the Z-scheme charge transfer path, the photo-generated electrons and holes are accumulated on the surface of BiO$_{2-x}$ nanosheets and Bi$_2$O$_{2.75}$ nanoparticles, respectively, and the excitons (the bound electron-hole pairs) are formed at the interface (Fig. 1(b)). After adding AgNO$_3$ solution, the positively charged Ag$^+$ is adsorbed on the surface of BiO$_{2-x}$ nanosheets by electrostatic attraction (Fig. 1(c)), which is further reduced to Ag^0 by the photo-generated electrons (Fig. 1(d)). Hence, compared with BiO-OVs (Fig. S1(a)), more fine particles can be observed on the surface of Ag/BiO$_{2-x}$/Bi$_2$O$_{2.75}$ (AgBO-3), as displayed in Fig. S1(b)-(c). Element mapping images (Fig. S1(d)) confirm the uniform distribution of Ag element without the obvious enrichment. Furthermore, as depicted in Fig. S1(e), with the increase in the amount of AgNO$_3$ introduced into the reaction system, Ag content in the prepared catalyst is also gradually increased from 3.62 wt% (AgBO-1) to 7.84 wt% (AgBO-3) and 12.27 wt % (AgBO-5), further indicating that Ag is successfully deposited on the surface of BiO$_{2-x}$/Bi$_2$O$_{2.75}$ under natural light irradiation.

In the HRTEM image of AgBO-3 (Fig. S2(a)-(b)), the lattice fringes with the interplanar spacing of 0.218 nm, 0.274 nm, 0.316 nm, 0.272 nm and 0.280 nm are in accordance with the ᴅ-space of the (200) crystal plane of Ag, (200) and (111) crystal planes of BiO$_{2-x}$, (110) and (103) crystal planes of Bi$_2$O$_{2.75}$, further demonstrating the co-existence of Ag, BiO$_{2-x}$ and Bi$_2$O$_{2.75}$ in the prepared composite. It can be clearly seen from the HRTEM images that Ag nanoparticles are mainly attached to the surface of BiO$_{2-x}$ nanosheets, suggesting the directional deposition of Ag. Moreover, since the reduction potential of Ag$^+$/Ag^0 (+0.7996 eV vs. NHE) is more negative than the conduction band potential of Bi$_2$O$_{2.75}$ (+1.83 eV vs. NHE) [32], Ag$^+$ cannot be reduced to Ag^0 by the photogenerated electrons of Bi$_2$O$_{2.75}$, which is in good accordance with the experimental results.

Due to the resonance effect of the localized electromagnetic fields between the metallic plasma Ag and BiO$_{2-x}$ enriched in oxygen vacancies, the significantly enhanced diffraction peaks of BiO$_{2-x}$ can be observed in the XRD patterns of Ag/BiO$_{2-x}$/Bi$_2$O$_{2.75}$ (Fig. S3(a)), while companying with the broadening and weakening of the Raman peaks (Fig. S3(b)) [33]. The characteristic peaks of Ag cannot be detected in the XRD patterns owing to its high dispersity and low content [23]. Moreover, compared with BiO-OVs, the obviously shifted Raman peaks of Ag/BiO$_{2-x}$/Bi$_2$O$_{2.75}$ is associated with the interfacial polarization charge transfer [34]. Further, the microscopic pore structure of the catalysts is characterized by N$_2$ adsorption-desorption isotherm curves, and the results are shown in Fig. S3(c). Obviously, all samples display the IV-type isotherm curves with H3 hysteresis loops, suggesting their mesoporous characteristics [35]. As the increase in Ag loading, the specific surface area of the catalysts is significantly decreased from 14.8778 cm^2•g^{-1} (BiO-OVs) to 6.5235 cm^2•g^{-1} (AgBO-1), 8.0751 cm^2•g^{-1} (AgBO-3) and 7.1588 cm^2•g^{-1} (AgBO-6) (Fig. S3(c)). The corresponding pore size distribution is depicted in Fig. S3(d). After coupling BiO-OVs with Ag, the total pore volume of BiO-OVs is also remarkably decreases from 0.11142 cm^3•g^{-1} to 0.07441 cm^3•g^{-1}
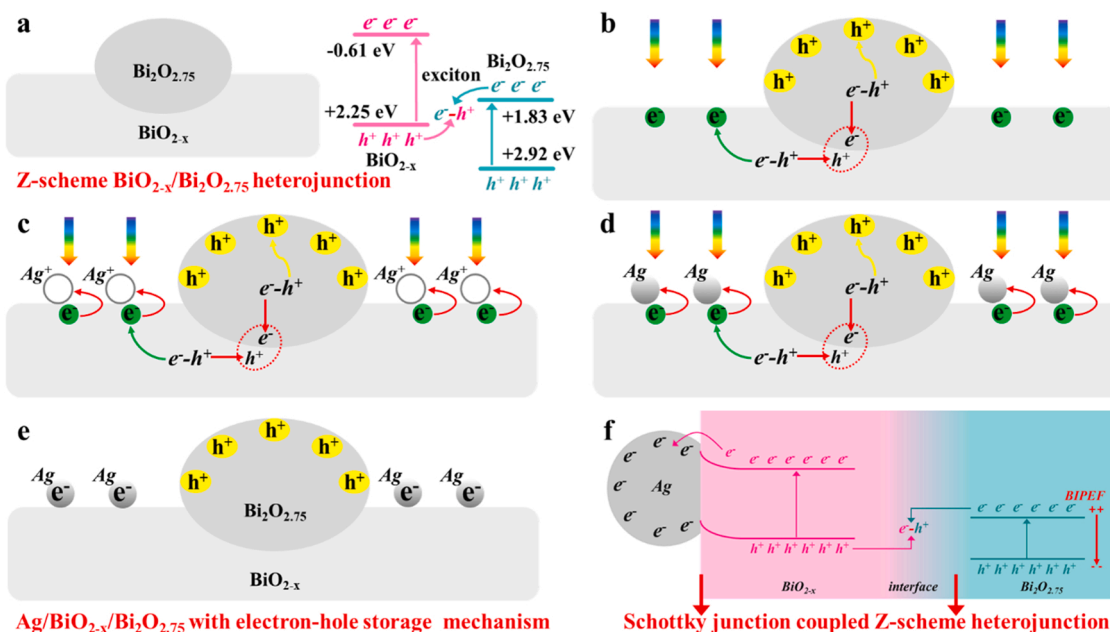
Fig. 1. The formation mechanism of Ag/BiO$_{2-x}$/Bi$_2$O$_{2.75}$ with electron-hole storage mechanism.

(AgBO-1), 0.04301 cm$^3 \cdot$g^{-1} (AgBO-3) and 0.04015 cm$^3 \cdot$g^{-1} (AgBO-6), while accompanying with the decrease in average pore size from 318.501 nm (BiO-OVs) to 293.032 nm (AgBO-1), 212.324 nm (AgBO-3) and 224.955 nm (AgBO-6). The reduced pore volume and average pore size are attributed to the deposition of Ag nanoparticles in the pores of BiO-OVs.

It can be seen from the XPS survey (Fig. S4(a)) that Ag/BiO$_{2-x}$/Bi$_2$O$_{2.75}$ is mainly consisted of Ag, Bi and O elements. In the high-resolution Ag 3d spectra (Fig. S4(b)), the characteristic peaks with a difference of 0.6 eV are assigned to Ag 3d$_{5/2}$ and Ag 3d$_{3/2}$ orbitals [15], respectively, further demonstrating that Ag$^+$ is successfully reduced to Ag^0 under natural light irradiation. Noticeably, the binding energies of Bi and O elements in AgBO-1, AgBO-3 and AgBO-6 show the visibly positive shifts in comparison with the pristine BiO-OVs (Fig. S4(c)-(d)). The positive shift of XPS characteristic peak represents the decrease in charge density [36], which means that the polarization charge will transfer from BiO-OVs to Ag, and stored in Ag nanoparticles (Fig. 1 (d)-(e)). Therefore, even though the partially exposed defects are covered by Ag nanoparticles, the EPR signals of Ag/BiO$_{2-x}$/Bi$_2$O$_{2.75}$ are not markedly weakened, and the resonance signal of AgBO-3 is even higher than that of the initial BiO-OVs (Fig. S4(e)).

The above polarization charge transfer process is further verified by theoretical calculations. It can be visibly observed from the charge density difference of Ag/BiO$_{2-x}$ that the electrons are accumulated and consumed on the side of Ag and BiO$_{2-x}$, respectively, corresponding to the decrease in the inner layer charge density of Bi and O atoms, and the increase in the interfacial charge density (Fig. S4(f)). Moreover, the work function of BiO$_{2-x}$ (4.12 eV) is smaller than that of Ag (4.23 eV), as shown in Fig. S5(a)-(b), substantiating its higher Fermi level and larger carrier concentration. Hence, after coupling Ag with BiO$_{2-x}$, the polarization charge of BiO$_{2-x}$ will spontaneously transfer to Ag driven by carrier concentration difference until their Fermi levels reach equilibrium [31]. The calculation results are well coincide with the variation tendency of XPS binding energies, further corroborating the plausibility of the conclusions related to polarization charge transfer.

The consumption of the free electrons in BiO$_{2-x}$ induces the upward energy band structure, and Schottky junction is constructed at Ag/BiO$_{2-x}$ interface (Fig. 1(f)) [37]. Concurrently, the strong ionic interaction between Ag and BiO$_{2-x}$ is triggered, corresponding the diffuse charge outline at the interface of Ag and BiO$_{2-x}$ in Fig. S5(c). The

construction of Schottky junction can efficiently suppress the recombination of electron-hole pairs induced by Coulomb interactions [38,39]. As a consequence, the electrons and holes are severally stored in Ag and Bi$_2$O$_{2.75}$, and Ag/BiO$_{2-x}$/Bi$_2$O$_{2.75}$ energy storage catalyst with the unique electron-hole storage mechanism is obtained by coupling Schottky junction with Z-scheme BiO$_{2-x}$/Bi$_2$O$_{2.75}$ heterojunction (Fig. 1 (e)-(f)).

3.2. Dark catalytic performance

The stored electron concentrations in the catalysts are estimated by the de-colorization experiments of methylene blue (MB, Fig. S6), and the de-colorization of each MB molecule corresponds to the consumption of two electrons (Eq. S(1)–(2)) [15,18]. The stored electron concentrations in AgBO-1 to AgBO-6 are calculated to be 45.06, 63.48, 86.55, 79.27, 55.24, and 37.39 μmol$\cdot$g^{-1}, which are 3.47–1.50 times higher than that of the initial BiO-OVs (24.94 μmol$\cdot$g^{-1}) (Fig. 2(a)).

The stored hole concentrations in the catalysts are estimated by spin quantum number (Eq. S(3)), which is obtained by EPR test. As shown in Fig. 1(b) and Table 1, the stored hole concentrations in AgBO-3 and AgBO-5 are calculated to be 0.0481 and 0.0215 μmol$\cdot$g^{-1}, respectively, which are 11.45 and 5.12 times higher than that of BiO-OVs (0.0042 μmol$\cdot$g^{-1}). Within 10 min of the simulated sunlight irradiation, 16.21, 11.17 and 7.379 μmol$\cdot$g^{-1} of the holes can be respectively produced by AgBO-3, AgBO-5 and BiO-OVs (Fig. 1(c) and Table 1). In comparison with BiO-OVs, the relatively higher hole concentrations in Ag/BiO$_{2-x}$/Bi$_2$O$_{2.75}$ are attributed to the more efficient charge separation and transfer, consistent with the larger photocurrent and the smaller charge transfer resistance (Fig. S7(a)-(b)). After stopping illumination for 10 min, the retained hole concentrations in AgBO-3 (2.763 μmol$\cdot$g^{-1}) and AgBO-5 (2.393 μmol$\cdot$g^{-1}) are still higher than that of BiO-OVs (1.440 μmol$\cdot$g^{-1}), as depicted in Fig. 1(c) and Table 1 further confirming the improvement of hole storage efficiency in Ag/BiO$_{2-x}$/Bi$_2$O$_{2.75}$. Notably, the stored hole concentrations in the catalysts are significantly lower than the concentration of the stored electrons, which is ascribed to the relatively poor hole storage ability of Bi$_2$O$_{2.75}$. In addition, the differences in test methods can also lead to certain errors.

The stored electrons and holes are continuously released after stopping illumination, leading to that the prepared Ag/BiO$_{2-x}$/Bi$_2$O$_{2.75}$ still exhibits appealing electrochemical properties in dark (Fig. S7(c)-(d) and
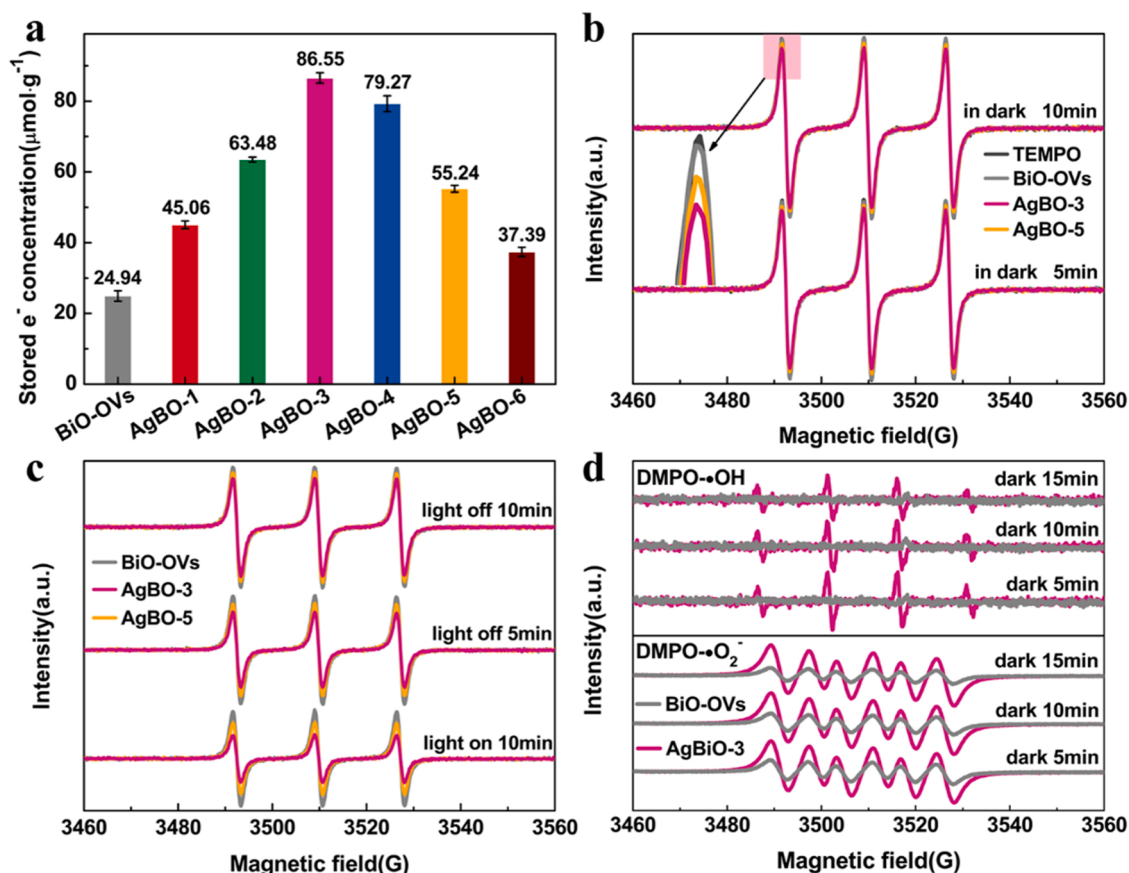
Fig. 2. (a) The stored electron concentrations in the catalysts obtained by MB de-colorization experiments; EPR spectra of BiO-OVs, AgBO-3 and AgBO-5: (b) in dark, (c) before and after illumination; (d) EPR spectra of DMPO-•O$_2^-$ and DMPO-•OH of BiO-OVs and AgBO-3 in dark.

Table 1
The calculated hole concentrations under different conditions based on EPR test results.

Samples	Dark 10 min	Light on 10 min	Light off 10 min
BiO-OVs	0.0042 μmol·g^{-1}	7.379 μmol·g^{-1}	1.440 μmol·g^{-1}
AgBO-3	0.0481 μmol·g^{-1}	16.21 μmol·g^{-1}	2.763 μmol·g^{-1}
AgBO-5	0.0215 μmol·g^{-1}	11.17 μmol·g^{-1}	2.393 μmol·g^{-1}

Fig. S8(a)-(b)). Due to the improvement of the electron-hole storage efficiencies, the higher concentrations of the active •O$_2^-$ and •OH radicals can be generated by Ag/BiO$_{2-x}$/Bi$_2$O$_{2.75}$ under dark condition (Fig. 1d).

The dark catalytic activity of the catalysts is evaluated by degrading organic pollutants under dark condition. The energy storage process has been completed during sample preparation. Hence, the synthesized Ag/BiO$_{2-x}$/Bi$_2$O$_{2.75}$ catalysts exhibit the markedly boosted dark catalytic performance without pre-illumination treatment, as shown in Fig. 3(a). After dark reaction for 32 min, only 30.96% of TC can be decomposed by BiO-OVs, and the corresponding degradation efficiency obtained by AgBO-3 is remarkably increased to 93.29% (Fig. 3(a)). The degradation rates of the catalysts to TC show an obvious trend of increasing first and decreasing later when the introduction amount of AgNO$_3$ is continuously increased, as shown in Fig. 3(b). The largest degradation rate is obtained by AgBO-3 (0.0828 min^{-1}), which is 7.96 times higher than that of BiO-OVs (0.0104 min^{-1}) (Fig. 3(b)). Subsequently, the gradually decreased dark reactivity is ascribed to the limited energy storage efficiency since the generation of free carriers and Ag loading amount are restricted by reaction time. Moreover, the particle size of Ag will gradually increase with the increase in Ag loading amount, and the resultant strong binding effect of Ag on electrons will affect the release of electrons and subsequent chemical reactions, resulting in the slow kinetic process.

In a completely dark environment, the successive and multiple cycle experiments are carried out to evaluate the stability and durability of the synthesized catalyst. During the 1st, 3rd, 6th and 9th cycle reactions, the degradation efficiencies of AgBO-3 to TC are 93.37%, 90.90%, 80.06% and 45.83%, respectively, while 73.28%, 66.84%, 50.08% and 38.56% of TOC can be removed, which signifies that AgBO-3 possesses the high reactivity and mineralization ability under dark condition (Fig. 3(c)). Impressively, the degradation activity of AgBO-3 to TC can maintain 10 runs, which means that the longstanding energy storage and the long-lasting dark catalytic activity can be achieved by coupling Ag with Z-scheme BiO$_{2-x}$/Bi$_2$O$_{2.75}$ heterojunction. With the prolonged reaction time, the vertiginous decrease in degradation efficiency of TC is ascribed to the rapid consumption of the stored electrons and holes. After pre-illumination treatment again, the long-lasting dark reactivity (10 runs) and high mineralization ability of AgBO-3 can be restored. As displayed in Fig. 3(d), 85.71% 85.14%, 63.24% and 45.22% of TC can be decomposed by AgBO-3 during the subsequent 1st, 3rd, 6th and 9th runs, and the corresponding TOC removal rates are 71.05%, 68.80%, 54.83% and 32.93%, respectively. Moreover, before and after cycle reactions, the XRD patterns (Fig. S9(a)), XPS spectra (Fig. S9(b)), SEM image (Fig. S9(c)-(d)) and TEM image (Fig. S9(e)-(f)) of AgBO-3 do not change significantly, and a larger number of the fine Ag particles can still be observed on the surface of the used catalyst (Fig. S9(d) and (f)), indicating that the prepared Ag/BiO$_{2-x}$/Bi$_2$O$_{2.75}$ heterojunction has the appealing structural stability, recyclability and repairability. As displayed in Fig. S9(g)-(i), the similar high-resolution XPS spectra of Ag, Bi and O elements before and after cycle reactions demonstrate that the
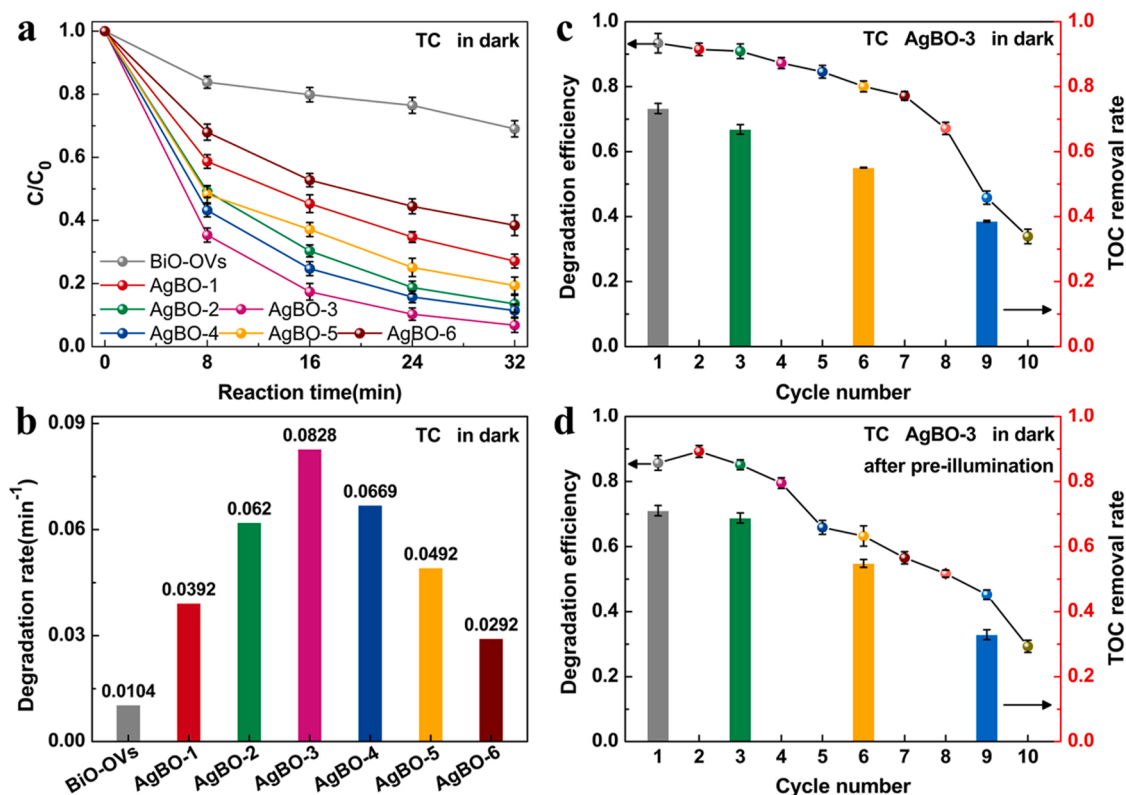
Fig. 3. (a) The degradation curves and (b) degradation rates of the catalysts to TC in dark; (c, d) the degradation efficiencies and TOC removal rates of AgBO-3 to TC during cycle reactions.
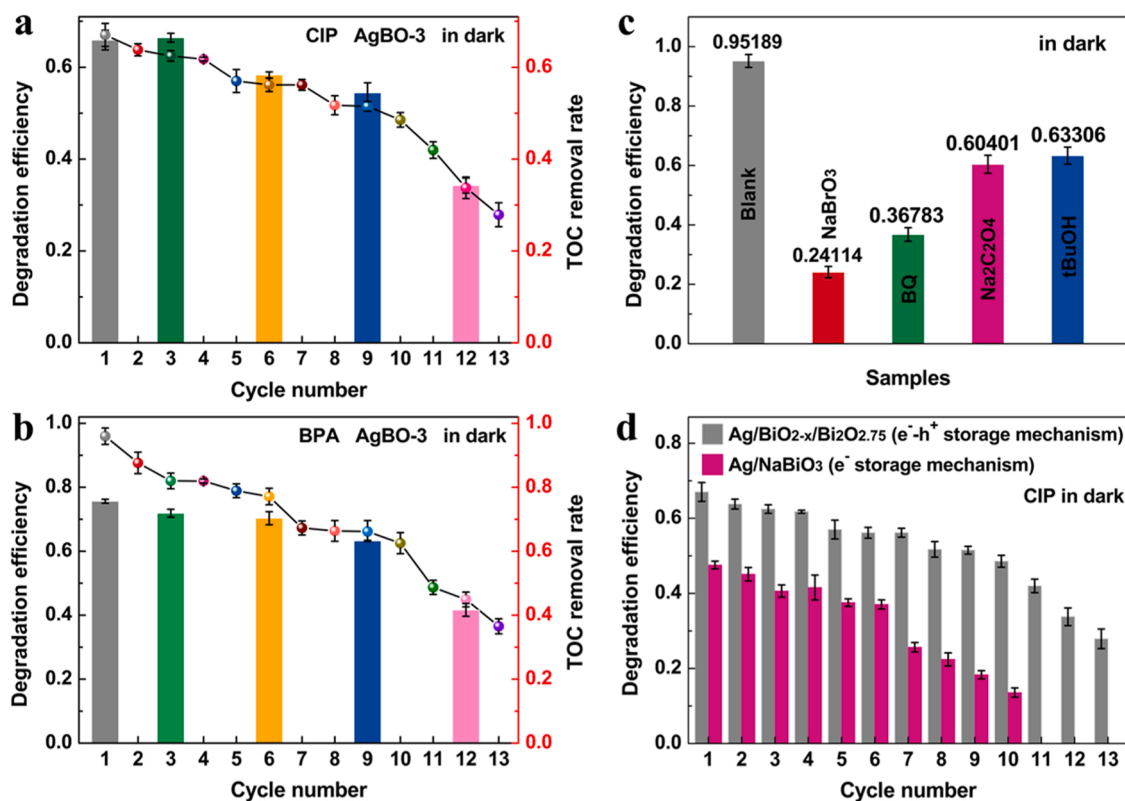

Fig. 4. The degradation efficiencies and TOC removal rates of AgBO-3 to (a) CIP and (b) BPA during cycle reactions; (c) active species trapping experiments in dark; (d) the comparison of CIP degradation efficiencies between Ag/BiO$_{2-x}$/Bi$_2$O$_{2.75}$ with electron-hole storage mechanism and Ag/NaBiO3 with the single electron storage mechanism.

surface elemental compositions of AgBO-3 can remain basically stable during reactions. After reactions, the increased binding energy of Ag elements is attributed to the consumption of the stored electrons in Ag, while the decrease in the binding energies of Bi and O elements corresponds to the consumption of the stored holes in $Bi_2O_{2.75}$. The results are in keeping with the electron-hole storage mechanism and dark catalytic processes.

In addition to TC, AgBO-3 also shows the long-lasting dark catalytic activity and high mineralization ability for multiple common pollutant sources (Fig. 4(a)-(b) and Fig. S10(a)-(c)). As depicted in Fig. 4(a)-(b), during the 1st, 3rd, 6th, 9th and 12th cycle reactions, the degradation efficiencies of CIP and BPA by AgBO-3 are 67.23%, 62.47%, 56.15%, 51.50%, 33.77% and 95.98%, 82.00%, 71.12%, 66.16, 44.92%, respectively, and the corresponding to the mineralization rates of 65.92%, 66.44%, 58.33%, 54.42%, 34.24% and 75.64%, 71.87%, 70.33%, 63.23%, 43.05%. Furthermore, as shown in Fig. S9(a)-(c),

95.19%, 95.77% and 93.00% of MO, AR and RhB can be decomposed by AgBO-3 within 30 min of dark catalytic reaction, and the corresponding cycle reactions can be maintained 10–12 periods. Active species trapping experiments (Fig. 4(c)) indicate the crucial role of e^-, h^+, $\bullet O_2^-$ and $\bullet OH$ radicals in the dark catalytic degradation for organic pollutants, which are in good consistent with the electron-hole storage mechanism. Owing to formation of the unique electron-hole storage mechanism, the degradation activity of $Ag/BiO_{2-x}/Bi_2O_{2.75}$ towards CIP is remarkably higher than that of $Ag/NaBiO_3$ with the single electron storage mechanism (Fig. 3(d)). Priors reports has confirmed the high dependence of CIP degradation on holes [23].

After dozens of runs, the characteristic bands of organic pollutants do not be detected in the FT-IR spectra of AgBO-3 (insets of Fig. S10(a)-(c), Fig. S11(a)-(d)), implying the surface adsorption of contaminates can be eliminated. Furthermore, besides TC and CIP, other small molecules or fragments can be identified in the corresponding degradation solutions

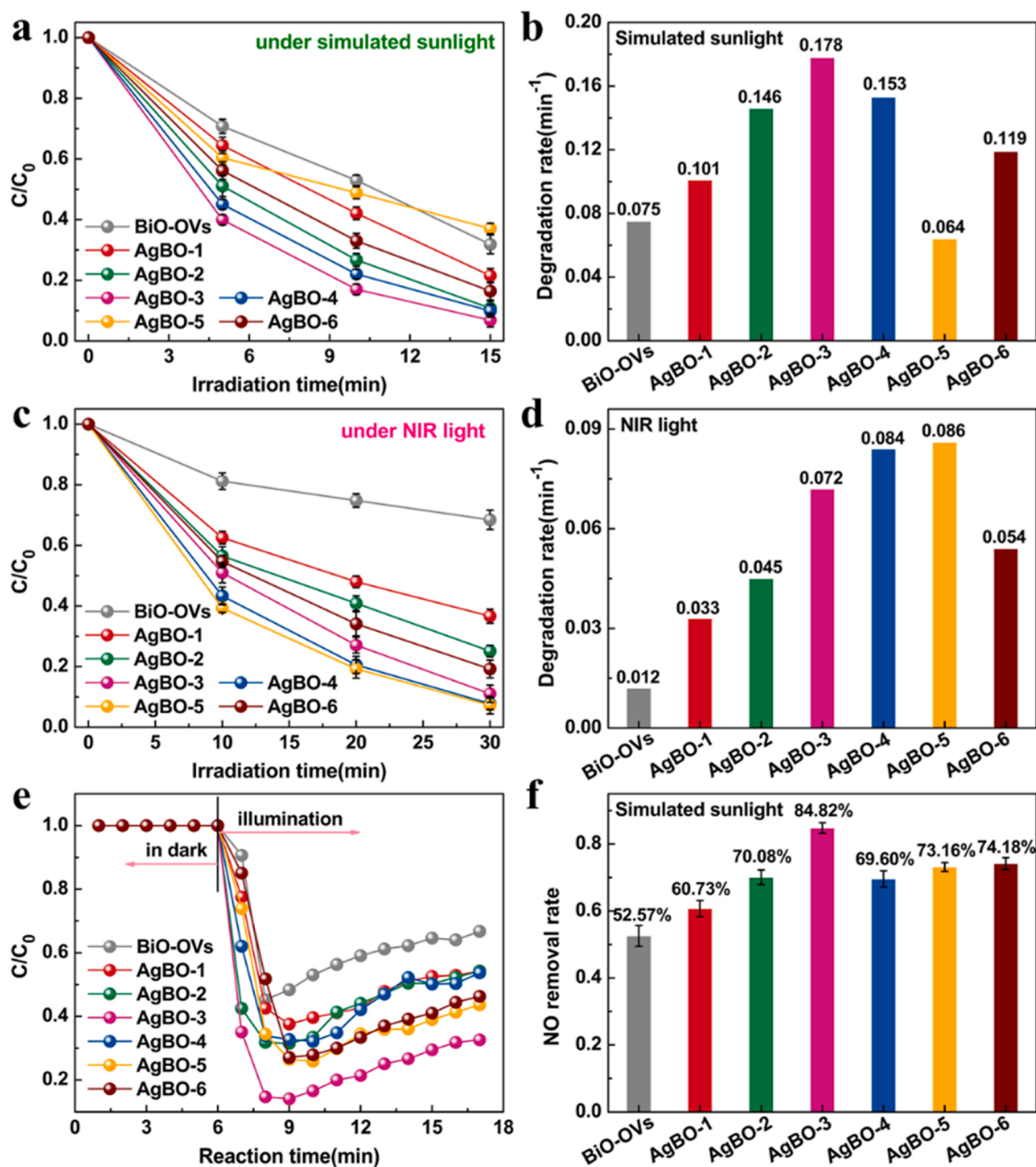

Fig. 5. The degradation curves and degradation rates of the catalysts to TC under (a, b) simulated sunlight and (c, d) NIR light irradiation; (e, f) NO removal curves and removal rates under simulated sunlight irradiation.

through LC-MS technology, as depicted in Fig. S12-17. Within 8 min of dark reaction, TC ($m/z = 445$) is transformed into intermediate products P1 ($m/z = 497$), P2 ($m/z = 477$) and P3 ($m/z = 475$) through the removal of the methyl group in the tertiary amino group, the hydroxylation and oxidation reactions of the tertiary amino group and the benzene ring, which can be further converted into products P4 ($m/z = 447$), P5 ($m/z = 437$), P6 ($m/z = 417$) through the removal of aldehyde group, hydroxyl and methyl groups, or products P4, P8 ($m/z = 391$), P9 ($m/z = 363$) and P11 ($m/z = 301$) by way of stepwise oxidation and cleavage reaction of benzene ring. The above products can be rapidly decomposed into other organic small molecules, corresponding to the appearance of the characteristic peaks at m/z of 60, 102, 123, 151 and so on (Fig. S12). After dark reaction for 24 min, the characteristic signal of TC disappears completely, accompanied with the appearance of some new substances ($m/z = 172$, 191 and 399) (Fig. S14–15), which means that TC is step-by-step decomposed during the dark reaction. The above analysis further substantiates that TC can be mineralized into H_2O, CO_2 or other small molecules by dark catalytic reaction rather than the simple surface adsorption. As shown in Fig. S18–19, the degradation and mineralization processes of TC and CIP mainly involve the substitution, oxidation and removal of the functional groups, as well as the ring-open and oxidative cracking reactions of the benzene rings, and the detailed degradation pathways are available in Supporting Information.

3.3. Full-spectrum driven photocatalytic activity

The full-solar-spectrum driven catalytic performance of the catalysts is evaluated by degrading TC and removing NO under simulated sunlight and NIR light irradiation. $Ag/BiO_{2-x}/Bi_2O_{2.75}$ exhibits the remarkably enhanced photocatalytic activities for both antibiotic degradation and NO removal. Within 15 and 30 min of the simulated sunlight and NIR light irradiation, TC can be completely decomposed by $Ag/BiO_{2-x}/Bi_2O_{2.75}$ (Fig. 5(a)-(b)), and the degradation rates obtained by the optimized heterojunction are 0.178 and 0.086 min^{-1}, respectively, which are 2.37 and 7.17 times higher than that of the pristine BiO-OVs (Fig. 5(c)-(d)). Furthermore, under simulated sunlight irradiation, the markedly enhanced NO removal activity is achieved by coupling Ag with $BiO_{2-x}/Bi_2O_{2.75}$ (Fig. 5(e)). The largest NO removal rate can reach as 84.82%, which is approximately 1.61 times higher than that of BiO-OVs (52.57%), as shown in Fig. 5(f). It is worth noting that, for NO removal experiments, the dark catalytic performance is almost undetectable, which is attributed to the dynamic reaction process for NO removal and the slow kinetic process of the stored carriers at the gas-solid interface.

Further, the photocatalytic NO oxidation pathways by the catalysts are analyzed by in-situ FT-IR spectra. Notably, the adsorption abilities of $Ag/BiO_{2-x}/Bi_2O_{2.75}$ to O_2, $\bullet O_2^-$ and $\bullet OH$ radicals are markedly improved due to the introduction of Ag enriched in electrons, corresponding to the enhanced adsorption peak and increased adsorption temperature in the TPD-O_2 curves (Fig. 6(a)), and increased adsorption energies in Table 2. Moreover, $Ag/BiO_{2-x}/Bi_2O_{2.75}$ also shows the enhanced chemisorption for polar NO molecule (Fig. 6(a)), which is ascribed to the separation of

Table 2
The adsorption energies of $\bullet O_2$ and $\bullet OH$ radicals on the surface of the different materials obtained by DFT calculations (the optimized structural modes are shown in Fig. S20).

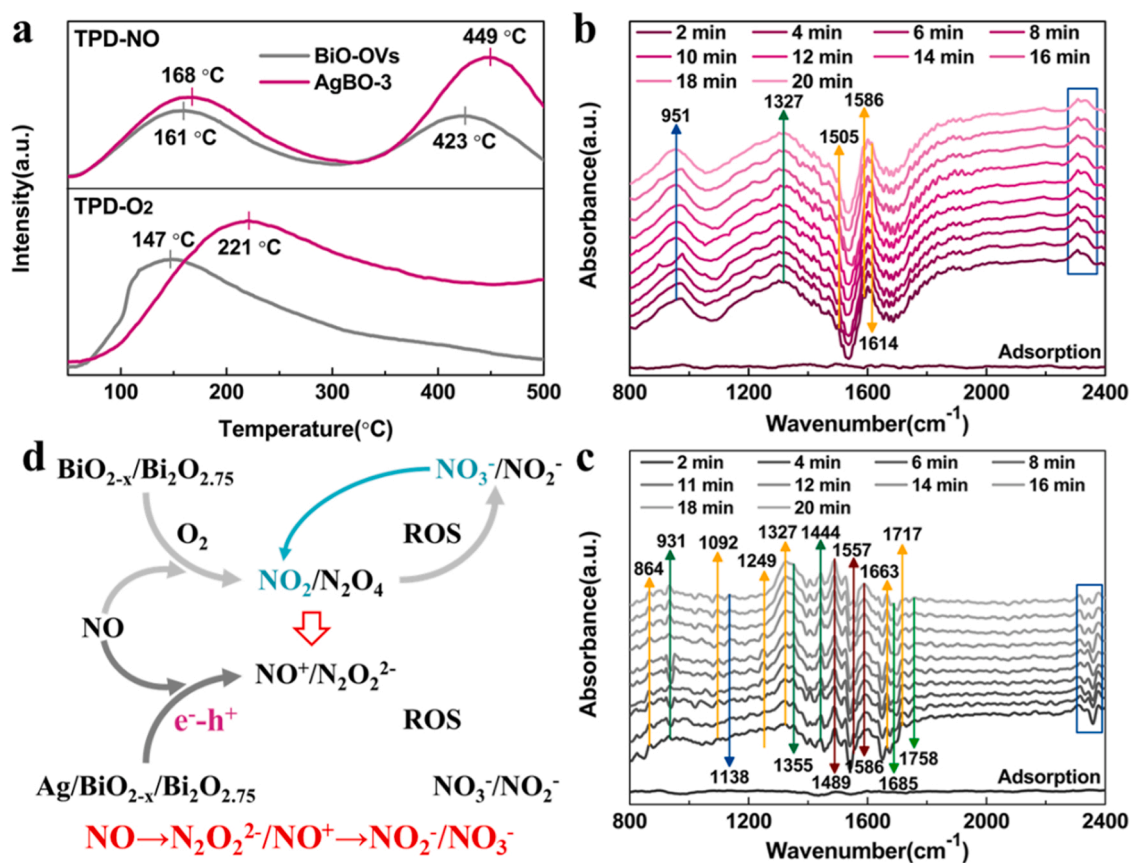| Species	BiO_{2-x}	$Bi_2O_{2.75}$	Ag/BiO_{2-x}	$Ag/Bi_2O_{2.75}$
$\bullet$ O_2 radical	4.23 eV	3.50 eV	5.45 eV	4.11 eV
$\bullet$ OH radical	4.51 eV	4.43 eV	6.08 eV	5.57 eV

Fig. 6. (a) TPD-NO and TPD-O_2 curves of BiO-OVs and AgBO-3; in-situ FT-IR spectra of (b) AgBO-3 and (c) BiO-OVs during photocatalytic NO oxidation; (d) photocatalytic NO oxidation pathways by $BiO_{2-x}/Bi_2O_{2.75}$ and $Ag/BiO_{2-x}/Bi_2O_{2.75}$.

positively charged and negatively charged centers induced by electron-hole storage mechanism. The absorption bands of $N_2O_2^{2-}$ (951 cm^{-1}) and NO^+ (2370–2270 cm^{-1}) can be detected in the in-situ FT-IR spectra of AgBO-3 (Fig. 5(b)) [40,41], which means that NO adsorbed on the surface of AgBO-3 is first activated to $N_2O_2^{2-}$ and NO^+ by capturing hot electrons and holes (Eqs. S(4)-(5)). Then, the intermediate products of $N_2O_2^{2-}$ and NO^+ is further oxidized to NO_2^- (1327 cm^{-1}) and NO_3^- (1614, 1586 and 1505 cm^{-1}) through Eq. S(6).

On the contrary, for BiO-OVs, NO is first oxidized to NO_2 and N_2O_4 by reacting with O_2 and •OH (Eq. S(7)-(8)), corresponding to the appearance of the absorption bands of NO_2 (1444, 1355 and 931 cm^{-1}) and N_2O_4 (1758 and 1685 cm^{-1}) in the in-situ FT-IR spectra of BiO-OVs (Fig. 6(c)) [42–46]. Subsequently, NO_2 and N_2O_4 are further oxidized to NO_2^- and NO_3^- by the hot electrons and the reactive oxygen species (ROS, including •O_2^- radical, •OH radical and $^1O_2$) (Eq. S(9)-(14)), corresponding to the appearance of the characteristic peaks of NO_2^- (1717, 1663, 1327, 1247, 1092 and 864 cm^{-1}) and NO_3^- (1586, 1557 and 1489 cm^{-1}) in Fig. 4(c) [43–45,47–49]. With the prolonged reaction time, the generated NO_3^- is reversely converted to the toxic NO_2 (Eq. S (15)) [50], resulting in that the characteristic peak of NO_3^- at 1586 cm^{-1} is gradually weakened, meanwhile companying with the gradual enhancement of the characteristic bands of NO_2 at 931 and 1355 cm^{-1}. In short, NO oxidation pathways is changed from $NO→NO_2/N_2O_4→NO_2^-/NO_3^-$ to $NO→N_2O_2^{2-}/NO^+→NO_2^-/NO_3^-$ (Fig. 6(d)) after coupling Ag with $BiO_{2-x}/Bi_2O_{2.75}$, which means that the generation of the toxic NO_2 is suppressed at the source (Fig. S21), and photocatalytic NO deep oxidation is achieved.

The markedly boosted full-spectrum-driven photocatalytic performance of the catalyst is ascribed to the light-induced LSPR excitation of the stored electrons and holes, and the resultant localized near-field enhancement effect. This point is further verified by the localized electric field (LEF) distributions of $Ag/BiO_{2-x}/Bi_2O_{2.75}$ obtained by finite-different time-domain (FDTD) simulated calculation. The used structural modes (Fig. S22(a)-(d)) and the corresponding information are available in Supporting Information. Two different excitation wavelengths of 535 nm and 1100 nm are chosen, corresponding to the transverse oscillation mode and longitudinal oscillation mode of the free carrier, respectively [51,52]. The results are shown in Fig. 7(a)-(b). The remarkably enhanced LEFs can be observed at edges of Ag and $BiO_{2-x}/Bi_2O_{2.75}$, which originates from the light-induced LSPR excitation of metal plasma and defects, concurrently corroborating the generation of the high-energy hot carriers. In evidence, the largest LEFs are distributed at the interfaces, which is attributed to the near-field plasmon energy transfer induced by the transverse oscillation of the free carriers [53–55]. For Ag/BiO_{2-x}, the maximum enhancement factor at 535 nm ($|E|^2/|E_0|^2 = 13.91$) is significantly larger than the value obtained at 1100 nm ($|E|^2/|E_0|^2 = 1.91$) (Fig. 7(a)), suggesting the leading role of transverse energy propagation. On the contrary, for $Ag/Bi_2O_{2.75}$, the maximum enhancement factor at 535 and 1100 nm are 2.07 and 2.99 (Fig. 7(b)), respectively, and the relatively larger enhancement factor at

1100 nm indicates the more important role of the longitudinal oscillation mode. In addition, for the entire $Ag/BiO_{2-x}/Bi_2O_{2.75}$ system, the largest maximum enhancement factor is obtained by Ag/BiO_{2-x} with the excitation wavelength of 535 nm, which demonstrates that transverse electron transfer cross Ag/BiO_{2-x} interface possesses the most crucial role for the light-induced chemical reactions.

Based on the above analysis, the enhancement mechanism of light-assisted catalytic reactions can be proposed. As shown in the UV–vis-NIR DRS (Fig. 8(a)), due to the synergistic LSPR effect between Ag and defects, $Ag/BiO_{2-x}/Bi_2O_{2.75}$ can make more full use of solar energy, corresponding the obviously red-shifted absorption edges and the significantly enhanced visible-NIR light absorption. In $Ag/BiO_{2-x}/Bi_2O_{2.75}$, electrons and holes are independently stored in Ag and $Bi_2O_{2.75}$, and the reverse electron flow from Ag to BiO_{2-x} is suppressed due to the existence of Schottky barrier. Upon illumination, as shown in Fig. 8(b), the stored electrons in Ag are excited to high-energy hot electrons (red electrons in Fig. 8(b)) owing to the LSPR effect of metal plasma Ag, while the stored holes in $Bi_2O_{2.75}$ are excited to high-energy hot holes (red holes in Fig. 8(b)) owing to the LSPR effect of defects [56, 57]. The produced hot electrons and hot holes can directly decompose organic pollutants and activate NO. At the same time, Z-scheme $BiO_{2-x}/Bi_2O_{2.75}$ heterojunction is excited, and the photo-generated electrons and holes are respectively accumulated on the conduction band position of BiO_{2-x} and the valence band position of $Bi_2O_{2.75}$, while a large number of excitons are generated at nano-scale coupled $BiO_{2-x}/Bi_2O_{2.75}$ interface by non-radiative decay. The photo-induced electrons of BiO_{2-x} can be transferred to Ag across the Schottky barrier to stabilize the generation of the hot electrons, and the photo-induced holes of $Bi_2O_{2.75}$ can compensate for hole consumption to stabilize hot hole density. The LSPR excitation of Ag and the resultant localized near-field enhancement effect can accelerate electron transition (green electromagnetic wave in Fig. 8(b)) and promote the interfacial charge transfer (red arrow in Fig. 8(b)) [53,54]. It can be clearly seen from the LEF distributions (Fig. 7) of $Ag/BiO_{2-x}/Bi_2O_{2.75}$ that the largest maximum enhancement factor is obtained by Ag/BiO_{2-x} at 535 nm, further substantiating that the photo-generated electrons of BiO_{2-x} can continuously transfer to Ag to stabilize its free charge density, and the high-energy hot electrons can be incessantly produced by plasma Ag.

Ultimately, •O_2^- and •OH radicals are generated by the redox reactions driven by the high-energy hot electrons of Ag and the high-energy hot holes of $Bi_2O_{2.75}$, as shown in Fig. 8(b). Since the electron transition and the interfacial charge transfer are simultaneously promoted by LSPR excitation, the separation efficiency of the photo-generated carriers of $Ag/BiO_{2-x}/Bi_2O_{2.75}$ is significantly improved, corresponding to the increase in photocurrent (Fig. S7(a)) and hole concentration (Fig. 8(c)), and the decrease in charge transfer resistance (Fig. S7(b)). Hence, in comparison with BiO-OVs, the higher concentrations of •O_2^- and •OH radicals can be produced by $Ag/BiO_{2-x}/Bi_2O_{2.75}$ through the redox reactions driven by the free high-energy hot carriers, which is in good consistent with the enhanced EPR signals
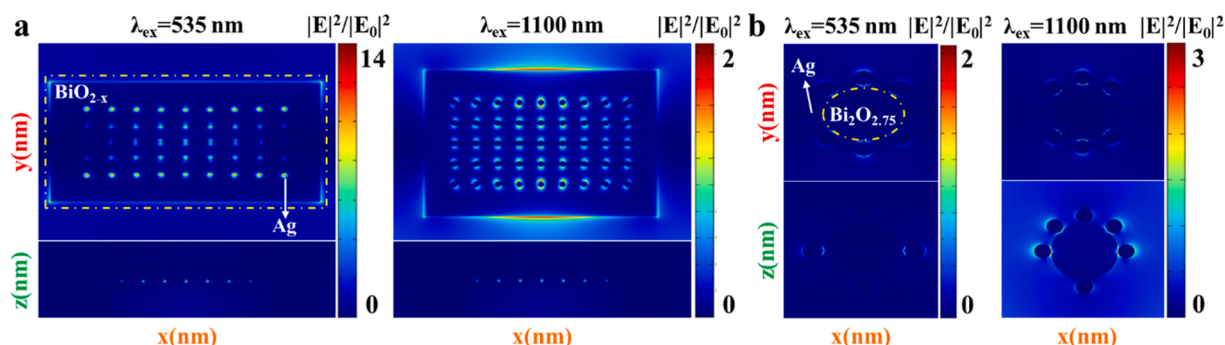

Fig. 7. The simulated electric field distributions of (a) Ag/BiO_{2-x} and (b) $Ag/Bi_2O_{2.75}$ with the excitation wavelength of 535 nm and 1100 nm.
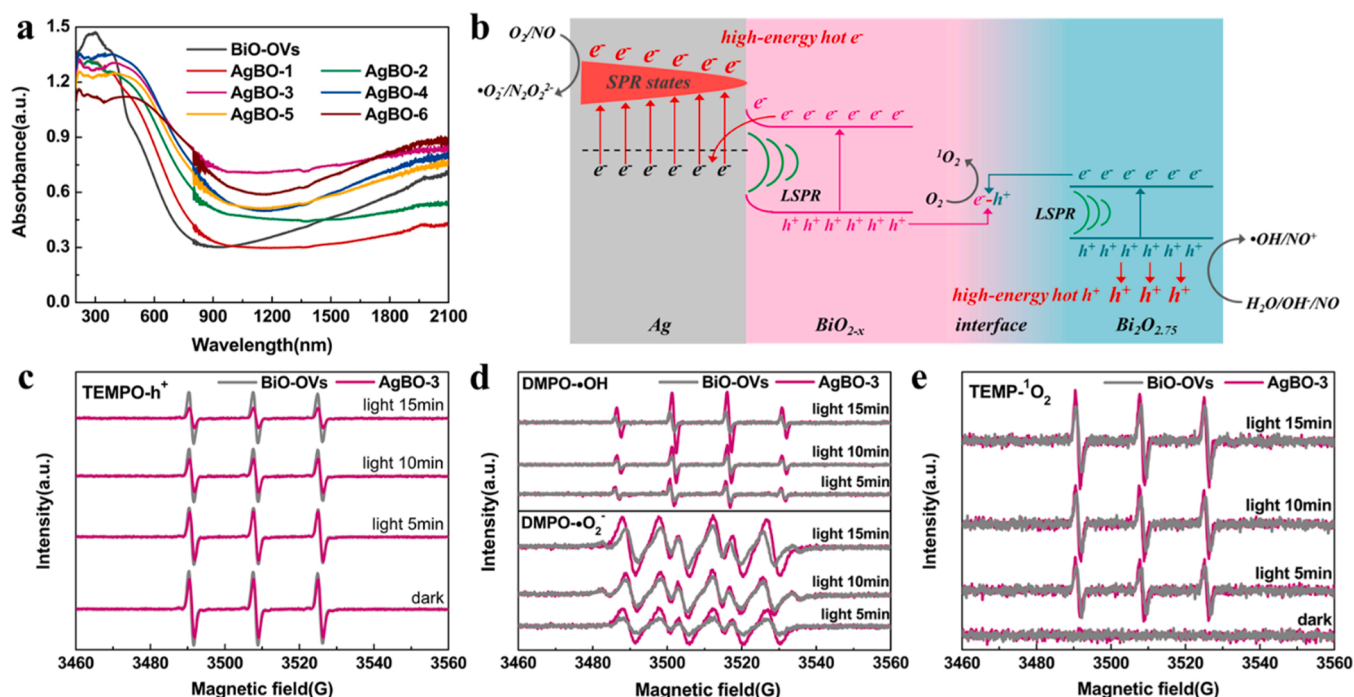
Fig. 8. a) UV–vis–NIR DRS; b) photochemical reactions of Ag/BiO$_{2-x}$/Bi$_2$O$_{2.75}$; EPR spectra of BiO-OVs and AgBO-3 under simulated sunlight irradiation: c) TEMPO-h$^+$, d) DMPO-•O$_2^-$ and DMPO-•OH, e) TEMP-^{1}O$_2$.

(Fig. 8(d)). Interestingly, the ^{1}O$_2$ concentration produced by Ag/BiO$_{2-x}$/Bi$_2$O$_{2.75}$ is also higher than that of BiO-OVs (Fig. 8(e)). The improvement in charge separation efficiency indicates that the bulk exciton effect of the catalyst is weakened. At the same time, combining with the increased concentrations of h$^+$ and •O$_2^-$, it can be ruled out that ^{1}O$_2$ is generated through the oxidation reaction between h$^+$ and •O$_2^-$ radical [58]. Therefore, for Ag/BiO$_{2-x}$/Bi$_2$O$_{2.75}$ system, ^{1}O$_2$ is produced by the exciton energy transfer process at BiO$_{2-x}$/Bi$_2$O$_{2.75}$ interface (Fig. 8(b)) [23,59]. Due to the Z-scheme charge transfer path of BiO$_{2-x}$/Bi$_2$O$_{2.75}$ heterojunction, the improvement in bulk charge separation efficiency induces the enhanced exciton effect at the interface and the increased ^{1}O$_2$ concentration. In other words, owing to the LSPR excitation of plasma Ag and defects, and the resultant localized near-field enhancement effect, the free carriers (e$^-$, h$^+$, •O$_2^-$ and •OH radicals) and exciton (^{1}O$_2$) regulated reaction processes are simultaneously promoted, leading to the markedly enhanced full-spectrum photocatalytic activity. The results of active species trapping experiments (Fig. S23 (a)-(c)) are good in consistence with the EPR tests, further indicating the rationality of the above light-induced chemical reactions. Furthermore, owing to the continuous energy input, under simulated sunlight irradiation, the concentrations of •O$_2^-$ and •OH radicals produced by the catalyst are significantly higher than that in the dark, as shown in Fig. S24, leading to the markedly increased TC degradation rate from 0.826 min^{-1} (in the dark) to 0.178 min^{-1} (simulated sunlight).

To sum up, the energy storage catalyst with the unique electron-hole storage mechanism is successfully obtained by coupling Schottky junction with Z-scheme junction. The energy storage efficiency is markedly improved due to the formation of Schottky and the capacitance nature of Ag, resulting in the boosted and long-acting dark catalytic activity. Moreover, the generation of ROS is promoted owing to the LSPR excitation of the stored electrons and holes and the resultant localized near-field enhancement effect, and the NO oxidation pathways is changed by activating NO molecule by the high-energy hot carriers, leading to the enhanced full-spectrum photocatalytic activity for antibiotic degradation and NO deep oxidation. Compared with other Bi-based or Ag-modified photocatalysts, as well as the commercial P25 (Table S2-3), Ag/BiO$_{2-x}$/Bi$_2$O$_{2.75}$ energy storage catalyst shows the relatively higher

reactive activity for antibiotic degradation and NO removal, indicating that it is a feasible strategy to obtain high-active and multifunctional catalysts for round-the-clock environmental cleaning through the synergistic integration of energy storage catalysis.

4. Conclusions

In summary, the synchronized enhancement of full-spectrum photocatalytic and dark catalytic activities is achieved through coupling Ag with Z-scheme BiO$_{2-x}$/Bi$_2$O$_{2.75}$ heterojunction. The prepared Ag/BiO$_{2-x}$/Bi$_2$O$_{2.75}$ exhibits the unique electron-hole storage mechanism. The recombination of electron-hole pairs is suppressed due to the formation of Schottky junction and the capacitance nature of Ag. Hence, the storage concentration of electrons and holes in Ag/BiO$_{2-x}$/Bi$_2$O$_{2.75}$ are respectively increased by 3.46 and 11.45 times compared with BiO$_{2-x}$/Bi$_2$O$_{2.75}$, resulting in the remarkably enhanced and long-lasting dark catalytic reactivity. Upon illumination, the electron transition and interfacial charge transfer are promoted due to the LSPR excitation and resultant localized near-field enhancement effect, and the high-energy hot electrons and hot holes can be continuously produced by plasma Ag and Bi$_2$O$_{2.75}$. Hence, the higher concentrations of active species can be generated by Ag/BiO$_{2-x}$/Bi$_2$O$_{2.75}$, leading to the significantly enhanced full-spectrum responsive catalytic activity for antibiotic degradation and NO deep oxidation. This work provides a win-win strategy to prepared high-active round-the-clock catalyst for environmental cleaning.

CRediT authorship contribution statement

Min Wang: Investigation, Methodology, Software, Writing – original draft, Visualization, Formal analysis, Validation, Data curation. **Guoqiang Tan:** Visualization, Supervision, Resources. **Bixin Zhang:** Data curation. **Yong Wang:** Data curation. **Yu Bi:** Writing – review & editing. **Qian Yang:** Validation. **Ying Liu:** Writing – review & editing. **Tian Liu:** Software. **Zeqiong Wang:** Investigation. **Huijun Ren:** Writing – review & editing, Validation, **Long Lv:** Validation. **Ao Xia:** Data curation. **Lixiong Yin:** Supervision. **Qibin Yuan:** Formal analysis. **Wenlong Liu:**

Software. **Yun Liu:** Supervision.

Declaration of Competing Interest

The authors declare that they have no known competing financial interests or personal relationships that could have appeared to influence the work reported in this paper.

Data Availability

Data will be made available on request.

Appendix A. Supporting information

Supplementary data associated with this article can be found in the online version at doi:10.1016/j.apcatb.2022.122052.

References

[1] H. Zhan, Q. Zhou, M. Li, R. Zhou, Y. Mao, P. Wang, Photocatalytic O_2 activation and reactive oxygen species evolution by surface B-N bond for organic pollutants degradation, Appl. Catal. B Environ. 310 (2022), 121329.

[2] H. Son, Y. Kim, Near-infrared driven photocatalyst (Ag/BiO_{2-x}) with post-illumination catalytic memory, J. Phys. Chem. Solids 167 (2022), 110781.

[3] C. Li, G. Zhao, T. Zhang, T. Yan, C. Zhang, L. Wang, L. Liu, S. Zhou, F. Jiao, A novel Ag@TiON/CoAl-layered double hydroxide photocatalyst with enhanced catalytic memory activity for removal of organic pollutants and Cr(VI), Appl. Surf. Sci. 504 (2020), 144352.

[4] C. Zhang, Y. Li, M. Li, D. Shuai, X. Zhou, X. Xiong, C. Wang, Q. Hu, Continuous photocatalysis via photo-charging and dark-discharging for sustainable environmental remediation: performance, mechanism, and influencing factors, J. Hazard. Mater. 420 (2021), 126607.

[5] T. Cai, Y. Liu, L. Wang, W. Dong, G. Zeng, Recent advances in round-the-clock photocatalytic system: mechanisms, characterization techniques and applications, J. Photochem. Photobiol. C Photochem. Rev. 39 (2019) 58–75.

[6] Q. Li, Y.W. Li, P. Wu, R. Xie, J.K. Shang, Palladium oxide nanoparticles on nitrogen-doped titanium oxide: accelerated photocatalytic disinfection and post-illumination catalytic "Memory", Adv. Mater. 20 (2008) 3717–3723.

[7] H. Chen, W. Fu, Y. Xing, J. Zhang, J. Ku, Engineering $SrCu_xO$ composition to tailor the degradation activity toward organic pollutant under dark ambient conditions, Environ. Sci. Pollut. Res. 26 (2019) 16449–16456.

[8] H. Chen, J. Motuzas, W. Martens, J.C. Diniz da Costa, Improved dark ambient degradation of organic pollutants by cerium strontium cobalt perovskite, J. Environ. Sci. (China) 90 (2020) 110–118.

[9] C. Wang, X. Liu, C. Chen, Enhanced photocatalytic property of graphene oxide/TiO_2 hybrids with WO_3 quantum dots, Integr. Ferroelectr. 190 (2018) 55–62.

[10] L.N. Li, Z.S. Liu, L.T. Guo, H.L. Fan, X.Y. Tao, $NaBiO_3/BiO_{2-x}$ composite photocatalysts with post-illumination "memory" activity, Mater. Lett. 234 (2019) 30–34.

[11] F. Feng, W. Yang, S. Gao, C. Sun, Q. Li, Postillumination activity in a single-phase photocatalyst of Mo-doped TiO_2 nanotube array from its photocatalytic "memory", ACS Sustain. Chem. Eng. 6 (2018) 6166–6174.

[12] L. Liu, W. Sun, W. Yang, Q. Li, J.K. Shang, Post-illumination activity of SnO_2 nanoparticle-decorated Cu_2O nanocubes by H_2O_2 production in dark from photocatalytic "memory", Sci. Rep. 6 (2016) 1–11.

[13] M. Wen, S. Song, Q. Liu, H. Yin, K. Mori, Y. Kuwahara, G. Li, T. An, H. Yamashit, Manipulation of plasmon-induced hot electron transport in Pd/MoO_{3-x}@ZIF-8: boosting the activity of Pd-catalyzed nitroaromatic hydrogenation under visible-light irradiation, Appl. Catal. B Environ. 282 (2021), 119511.

[14] F. Yi, J. Ma, C. Lin, H. Zhang, Y. Qian, H. Jin, K. Zhang, Electronic and thermal transfer actuating memory catalysis for organic removal by a plasmonic photocatalyst, Chem. Eng. J. 427 (2022), 132028.

[15] T. Cai, Y. Liu, L. Wang, S. Zhang, J. Ma, W. Dong, Y. Zeng, J. Yuan, C. Liu, S. Luo, "Dark deposition" of Ag nanoparticles on TiO_2: improvement of electron storage capacity to boost "memory catalysis" activity, ACS Appl. Mater. Interfaces 10 (2018) 25350–25359.

[16] Y. Zhang, Q. Li, C. Liu, X. Shan, X. Chen, W. Dai, X. Fu, The promoted effect of a metal-organic frameworks (ZIF-8) on Au/TiO_2 for CO oxidation at room temperature both in dark and under visible light irradiation, Appl. Catal. B Environ. 224 (2018) 283–294.

[17] L. Wu, Z. Zhao, H. Yu, H. Wang, G. Li, H. Li, J. Yan, A strong hydrangea-like Au-TiO_2 catalyst for round-the-clock degradation of oxalic acid in the presence of ozone, Catal. Sci. Technol. 10 (2020) 7481–7485.

[18] A. Takai, P.V. Kamat, Capture, store, and discharge. Shuttling photogenerated electrons across TiO_2-silver interface, ACS Nano 5 (2011) 7369–7376.

[19] Y. Choi, M.S. Koo, A.D. Bokare, D.H. Kim, D.W. Bahnemann, W. Choi, Sequential process combination of photocatalytic oxidation and dark reduction for the removal of organic pollutants and Cr(VI) using Ag/TiO_2, Environ. Sci. Technol. 51 (2017) 3973–3981.

[20] K. Yu, R. Wei, S. Yang, H. Guo, H. Hua, C. Sun, X. Luo, Dark formation of reactive oxygen species by bifunctional copper doped sodium bismuthate: direct oxidation vs catalytic oxidation of organic pollutants, J. Hazard. Mater. 406 (2021), 124297.

[21] Z. Wu, K. Guo, S. Cao, W. Yao, L. Piao, Synergetic catalysis enhancement between H_2O_2 and TiO_2 with single-electron-trapped oxygen vacancy, Nano Res. 13 (2020) 551–556.

[22] L. Zeng, W. Song, M. Li, D. Zeng, C. Xie, Catalytic oxidation of formaldehyde on surface of $HTiO_2/HCTiO_2$ without light illumination at room temperature, Appl. Catal. B Environ. 147 (2014) 490–498.

[23] M. Wang, G. Tan, S. Feng, L. Yin, Y. Wang, B. Zhang, L. Lv, H. Ren, Construction of Ag/$NaBiO_3$ with dual active sites for photocatalytic NO deep oxidation and long-lasting organic pollutants degradation in the dark, J. Hazard. Mater. 416 (2021), 125877.

[24] M. Su, H. Sun, Z. Tian, Z. Zhao, P. Li, Z-scheme 2D/2D WS_2/Bi_2WO_6 heterostructures with enhanced photocatalytic performance, Appl. Catal. A Gen. 631 (2022), 118485.

[25] J. Zhao, M. Ji, H. Chen, Y.X. Weng, J. Zhong, Y. Li, S. Wang, Z. Chen, J. Xia, H. Li, Interfacial chemical bond modulated $Bi_{19}S_{27}Br_3$/g-C_3N_4 Z-scheme heterojunction for enhanced photocatalytic CO_2 conversion, Appl. Catal. B Environ. 307 (2022), 121162.

[26] F. Mo, Q. Zhou, Y. He, Nano-Ag: environmental applications and perspectives, Sci. Total Environ. 829 (2022), 154644.

[27] W. Kong, Z. Xing, B. Fang, Y. Cui, Z. Li, W. Zhou, Plasmon Ag/Na-doped defective graphite carbon nitride/NiFe layered double hydroxides Z-scheme heterojunctions toward optimized photothermal-photocatalytic-Fenton performance, Appl. Catal. B Environ. 304 (2022), 120969.

[28] J. Cai, J. Huang, S. Wang, J. Iocozzia, Z. Sun, J. Sun, Y. Yang, Y. Lai, Z. Lin, Crafting mussel-inspired metal nanoparticle-decorated ultrathin graphitic carbon nitride for the degradation of chemical pollutants and production of chemical resources, Adv. Mater. 31 (2019), 1806314.

[29] Y. Liu, S. Cheng, S. Zhan, X. Wu, Manipulating energy transfer in UCNPs@SiO_2@Ag nanoparticles for efficient infrared photocatalysis, Inorg. Chem. 60 (2021) 5704–5710.

[30] M. Wang, G. Tan, D. Zhang, B. Li, L. Lv, Y. Wang, H. Ren, X.L. Zhang, A. Xia, Y. Liu, Defect-mediated Z-scheme $BiO_{2-x}/Bi_2O_{2.75}$ photocatalyst for full spectrum solar-driven organic dyes degradation, Appl. Catal. B Environ. 254 (2019) 98–112.

[31] M. Wang, G. Tan, M. Dang, Y. Wang, B. Zhang, H. Ren, L. Lv, A. Xia, W. Liu, Y. Liu, Double build-in electric fields mediated double Z-scheme semiconductor-nonmetal plasma heterojunction for dark-full-spectrum-driven environmental clean, Appl. Surf. Sci. 533 (2020), 147565.

[32] K. Wenderich, G. Mul, Methods, mechanism, and applications of photodeposition in photocatalysis: a review, Chem. Rev. 116 (2016), 145873-14619.

[33] Y. Wang, G. Tan, B. Li, M. Dang, L. Lv, M. Wang, D. Zhang, H. Ren, A. Xia, Enhanced NIR photocatalytic of Ag-RGO@{010}BiVO_4/RGO@{110}BiVO_4 photocatalysts induced by resonance effect of transverse electric of RGO and transverse magnetic of Ag, Appl. Surf. Sci. 489 (2019) 1–12.

[34] R. Feng, W. Lei, X. Sui, X. Liu, X. Qi, K. Tang, G. Liu, M. Liu, Anchoring black phosphorus quantum dots on molybdenum disulfide nanosheets: a 0D/2D nanohybrid with enhanced visible- and NIR-light photoactivity, Appl. Catal. B Environ. 238 (2018) 444–453.

[35] F. Wang, T. Li, T. Li, L. Xia, Coupling of CdS and g-C_3N_4 decorated dendritic fibrous nano-silica for efficient photocatalytic reduction of uranium (VI), Sep. Purif. Technol. 299 (2022), 121707.

[36] C. Qi, H. Chen, X. Chen, C. Chu, X. Mei, W. Lu, N. Li, In-situ-reduced synthesis of cyano group modified g-C_3N_4/$CaCO_3$ composite with highly enhanced photocatalytic activity for nicotine elimination, J. Environ. Sci. 126 (2023) 517–530.

[37] Y. Zhang, J. Liu, Y.S. Kang, X.L. Zhang, Silver based photocatalysts in emerging applications, Nanoscale (2022) 11909–11922.

[38] O. Altan, E. Kalay, The influence of band bending phenomenon on photocatalytic Suzuki-Miyaura coupling reaction: the case of AgPd alloy nanoparticles supported on graphitic carbon nitride, Appl. Surf. Sci. 580 (2022), 152287.

[39] X. Zhang, J. Yan, F. Zheng, J. Zhao, L.Y.S. Lee, Designing charge transfer route at the interface between WP nanoparticle and g-C_3N_4 for highly enhanced photocatalytic CO_2 reduction reaction, Appl. Catal. B Environ. 286 (2021), 119879.

[40] Y. Tan, S. Wei, X. Liu, B. Pan, S. Liu, J. Wu, M. Fu, Y. Jia, Y. He, Neodymium oxide (Nd_2O_3) coupled tubular g-C_3N_4, an efficient dual-function catalyst for photocatalytic hydrogen production and NO removal, Sci. Total Environ. 773 (2021), 145583.

[41] P. Chen, H. Wang, H. Liu, Z. Ni, J. Li, Y. Zhou, F. Dong, Directional electron delivery and enhanced reactants activation enable efficient photocatalytic air purification on amorphous carbon nitride co-functionalized with O/La, Appl. Catal. B Environ. 242 (2019) 19–30.

[42] G. Cheng, X. Liu, X. Song, X. Chen, W. Dai, R. Yuan, X. Fu, Visible-light-driven deep oxidation of NO over Fe doped TiO_2 catalyst: Synergic effect of Fe and oxygen vacancies, Appl. Catal. B Environ. 277 (2020), 119196.

[43] J. Zhang, H. Tao, S. Wu, J. Yang, M. Zhu, Enhanced durability of nitric oxide removal on TiO_2 (P25) under visible light: Enabled by the direct Z-scheme mechanism and enhanced structure defects through coupling with C_3N_5, Appl. Catal. B Environ. 296 (2021), 120372.

[44] H. Wu, C. Yuan, R. Chen, J. Wang, F. Dong, J. Li, Y. Sun, Mechanisms of interfacial charge transfer and photocatalytic NO oxidation on $BiOBr/SnO_2$ p-n Heterojunctions, ACS Appl. Mater. Interfaces 12 (2020) 43741–43749.

[45] P. Chen, H. Liu, Y. Sun, J. Li, W. Cui, L. Wang, W. Zhang, X. Yuan, Z. Wang, Y. Zhang, F. Dong, Bi metal prevents the deactivation of oxygen vacancies in $Bi_2O_2CO_3$ for stable and efficient photocatalytic NO abatement, Appl. Catal. B Environ. 264 (2020), 118545.

[46] Q. Chen, H. Long, M. Chen, Y. Rao, X. Li, Y. Huang, In situ construction of biocompatible Z-scheme α-Bi_2O_3/$CuBi_2O_4$ heterojunction for NO removal under visible light, Appl. Catal. B Environ. 272 (2020), 119008.

[47] J. Nie, J. Gao, Q. Shen, W. Zhang, F. Rao, M. Hojamberdiev, Flower-like $Bi/CeO_{2-\delta}$ plasmonic photocatalysts with enhanced visible-light-induced photocatalytic activity for NO removal, Sci. China Mater. 63 (2020) 2272–2280.

[48] Y. Ren, Y. Li, X. Wu, J. Wang, G. Zhang, S-scheme Sb_2WO_6/g-C_3N_4 photocatalysts with enhanced visible-light-induced photocatalytic NO oxidation performance, Chin. J. Catal. 42 (2020) 69–77.

[49] M. Sun, W. Zhang, Y. Sun, Y. Zhang, F. Dong, Synergistic integration of metallic Bi and defects on BiOI: Enhanced photocatalytic NO removal and conversion pathway, Chin. J. Catal. 40 (2019) 826–836.

[50] W. Zhang, Y. Wang, Y. Wang, Y. Liang, F. Dong, Highly efficient photocatalytic NO removal and in situ DRIFTS investigation on $SrSn(OH)_6$, Chin. Chem. Lett. (2021) 7–10.

[51] M. Rycenga, C.M. Cobley, J. Zeng, W. Li, C.H. Moran, Q. Zhang, D. Qin, Y. Xia, Controlling the synthesis and assembly of silver nanostructures for plasmonic applications, Chem. Rev. 111 (2011) 3669–3712.

[52] H. Tian, X. Liu, Z. Liang, P. Qiu, X. Qian, H. Cui, J. Tian, Gold nanorods/g-C_3N_4 heterostructures for plasmon-enhanced photocatalytic H_2 evolution in visible and near-infrared light, J. Colloid Interface Sci. 557 (2019) 700–708.

[53] Z. Zhang, J. Huang, Y. Fang, M. Zhang, K. Liu, B. Dong, A nonmetal plasmonic Z-scheme photocatalyst with UV- to NIR-driven photocatalytic protons reduction, Adv. Mater. 29 (2017), 1606688.

[54] Z. Xu, Y. Lin, M. Yin, H. Zhang, C. Cheng, L. Lu, X. Xue, H.J. Fan, X. Chen, D. Li, Understanding the enhancement mechanisms of surface plasmon-mediated photoelectrochemical electrodes: a case study on Au nanoparticle decorated TiO_2 nanotubes, Adv. Mater. Interfaces 2 (2015), 1500169.

[55] H. Ren, J.L. Yang, W.M. Yang, H.L. Zhong, J.S. Lin, P.M. Radjenovic, L. Sun, H. Zhang, J. Xu, Z.Q. Tian, J.F. Li, Core-shell-satellite plasmonic photocatalyst for broad-spectrum photocatalytic water splitting, ACS Mater. Lett. 3 (2021) 69–76.

[56] Y. Li, M. Wen, Y. Wang, G. Tian, C. Wang, J. Zhao, Plasmonic hot electrons from oxygen vacancies for infrared light-driven catalytic CO_2 reduction on Bi_2O_{3-x}, Angew. Chem. Int. Ed. 60 (2021) 910–916.

[57] L. Shi, W. Zhou, Z. Li, S. Koul, A. Kushima, Y. Yang, Periodically ordered nanoporous perovskite photoelectrode for efficient photoelectrochemical water splitting, ACS Nano 12 (2018) 6335–6342.

[58] X. Li, W. Zhang, W. Cui, J. Li, Y. Sun, G. Jiang, H. Huang, Y. Zhang, F. Dong, Reactant activation and photocatalysis mechanisms on Bi-metal@Bi_2GeO_5 with oxygen vacancies: a combined experimental and theoretical investigation, Chem. Eng. J. 370 (2019) 1366–1375.

[59] H. Wang, X. Sun, D. Li, X. Zhang, S. Chen, W. Shao, Y. Tian, Y. Xie, Boosting hot-electron generation: exciton dissociation at the order-disorder interfaces in polymeric photocatalysts, J. Am. Chem. Soc. 139 (2017) 2468–2473.